Transient Density-Induced Dipolar Interactions in a Thin Vapor Cell

Florian Christaller,[1] Max Mäusezahl,[1] Felix Moumtsilis,[1] Annika Belz,[1,2] Harald Kübler,[1] Hadiseh Alaeian,[3] Charles S. Adams,[2] Robert Löw,[1] and Tilman Pfau[1,*]

[1]*5. Physikalisches Institut and Center for Integrated Quantum Science and Technology, Universität Stuttgart, Pfaffenwaldring 57, 70569 Stuttgart, Germany*

[2]*Department of Physics, Joint Quantum Centre (JQC) Durham-Newcastle, Durham University, South Road, Durham DH1 3LE, United Kingdom*

[3]*Elmore Family School of Electrical and Computer Engineering, Department of Physics and Astronomy, Purdue Quantum Science and Engineering Institute, Purdue University, West Lafayette, Indiana 47907, USA*

(Received 4 October 2021; revised 11 February 2022; accepted 23 March 2022; published 27 April 2022)

We exploit the effect of light-induced atomic desorption to produce high atomic densities ($n \gg k^3$) in a rubidium vapor cell. An intense off-resonant laser is pulsed for roughly one nanosecond on a micrometer-sized sapphire-coated cell, which results in the desorption of atomic clouds from both internal surfaces. We probe the transient atomic density evolution by time-resolved absorption spectroscopy. With a temporal resolution of $\approx$ 1 ns, we measure the broadening and line shift of the atomic resonances. Both broadening and line shift are attributed to dipole-dipole interactions. This fast switching of the atomic density and dipolar interactions could be the basis for future quantum devices based on the excitation blockade.

DOI: 10.1103/PhysRevLett.128.173401

The effect of dipole-dipole interactions in optical media becomes important when the density n is significantly larger than the wave number cubed k^3 of the interaction light field. Entering this regime leads to interesting nonlinear effects such as an excitation blockade [1], nonclassical photon scattering [2], self-broadening (collisional broadening) [3], and the collective Lamb shift [4,5].

Dipole-dipole interactions are observable in steady-state experiments performed in thin alkali vapor cells [6–8], where the cells are heated to temperatures above 300 °C. Dipolar broadening effects were previously observed to be independent of the system geometry, while the line shift depends on the dimensionality of the system, as investigated in a 2D model [8,9]. It is however not straightforward to prepare high densities with alkali vapors [10].

One technique to increase the atomic density is light-induced atomic desorption (LIAD) [11–16] or light-activated dispensers [17]. LIAD is commonly used for loading magneto-optical traps [18–20] and has been studied in confined geometries like photonic-band gap fibers [21,22] or porous samples [23]. However, the application of pulsed LIAD for fast switching of dipole-dipole interactions is so far unexplored.

In our pulsed LIAD setup, we can switch the atomic density in the nanosecond domain, which allows one to study the dipole-dipole interaction on a timescale faster than the natural atomic lifetime. This fast density switching has been already used in our group to realize an on-demand room-temperature single-photon source based on the Rydberg blockade [24]. In this Letter, we study the dipolar interaction for the two transitions D_1: $5S_{1/2} \rightarrow 5P_{1/2}$ and D_2: $5S_{1/2} \rightarrow 5P_{3/2}$ of rubidium with different transition dipole moments.

We first describe our LIAD measurement results in a thicker part of the cell [cell thickness $L = 6.24(7)$ μm] at a low density ($nk^{-3} \approx 1$). This measurement is used as the basis to set up a model for the velocity and density distribution of the desorbed atoms. Then, we focus on a thinner part of the cell [$L = 0.78(2)$ μm], where we can study transient density-dependent dipolar interactions at a high density (up to $nk^{-3} \approx 100$). To this end, we compare two transitions (D_1 and D_2 transition of rubidium) with different transition dipole moments to investigate their influences on the dipole-dipole interaction in a quasi-2D geometry ($L \approx \lambda_{\text{probe}}$).

We use a self-made, wedge-shaped, micrometer-sized cell with an attached reservoir tube filled with rubidium (72% ^{85}Rb, 28% ^{87}Rb), shown in Fig. 1(b). By heating the cell independently from the reservoir, we can produce a certain rubidium coverage on the cell walls and a vapor pressure in the cell with a comparably small background density $n \approx 10^{14}$ cm^{-3} (reservoir temperature $T_{\text{res}} \approx 180$ °C). In our setup, the pulsed LIAD laser and the probe laser are aligned collinearly in front of the cell [Fig. 1(a)]. The pulsed LIAD laser at 532 nm has a pulse length of 1.1(1) ns (FWHM) and a repetition rate of 50 kHz. This off-resonant pulse leads to the desorption of rubidium atoms bound to the sapphire-coated glass surface. The amount of desorbed atoms depends on the peak intensity I of the LIAD pulse. We probe the desorbed atoms at 795 nm (D_1 transition of Rb) or 780 nm (D_2 transition of Rb). Both probe lasers have an intensity well

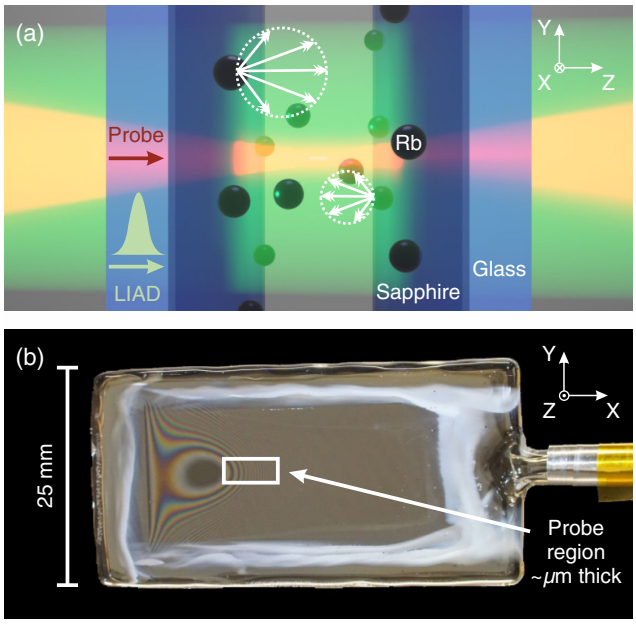

FIG. 1. (a) Illustration of the LIAD process. A green laser pulse (LIAD pulse) desorbs rubidium (Rb) atoms, which are adsorbed on the inner, sapphire-coated surface of the glass cell. The desorbed atoms are emitted with a certain velocity distribution into the cell volume from both sides of the cell, where they are probed with a red laser (probe laser). (b) Photo of the wedge-shaped micrometer-sized cell with interference fringes (Newton's rings). The cell thickness in the probe region is determined interferometrically and ranges from 0.78(2) to 6.24(7) μm from left to right.

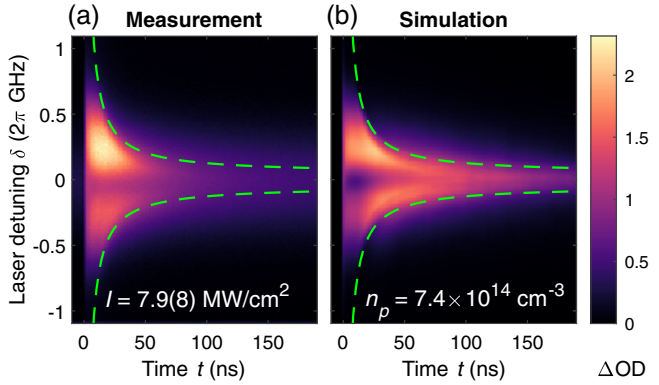

FIG. 2. (a) Measured ΔOD map of the ^{85}Rb $F_g = 2$ transition of the D_2 line. After the atoms, depending on their detuning (z velocity), hit the other cell wall the signal decreases. The TOF(δ) is shown with two dashed green lines. The intensity I is the peak intensity of the LIAD pulse. The cell thickness is $L = 6.24(7)$ μm, and the reservoir temperature is $T_{\mathrm{res}} \approx 140\,^{\circ}\mathrm{C}$. (b) Simulated ΔOD map of desorbed atoms. The simulation parameters are adapted to the measurement. The TOF(δ) curves (dashed green lines) are plotted, too. The indicated n_p is the peak density at 2 ns.

below the resonant D_2 saturation intensity $I_{\mathrm{probe}} < 0.01 I_{\mathrm{sat},D_2}$. The measured Gaussian beam waist radius ($1/e^2$) of the probe laser is $w_{\mathrm{probe}} = 2.0(2)$ μm, while the LIAD laser has a waist radius of $w_{\mathrm{LIAD}} = 13.7(1)$ μm. We measure the transmitted photons with a single-photon counting module, which is read out by a time tagger module. Our wedge-shaped cell has a point of contact of the cell walls, which can be seen in Fig. 1(b) as a dark circle. To the right of this point lies the probe region where the cell is less than 10 μm thick. The local cell thickness can be directly determined interferometrically by counting Newton's rings.

During the measurement, the probe laser is scanned over the D_1 or D_2 transition at a slow frequency of 11 Hz. At the same time, the LIAD laser sends pulses with a high repetition rate (50 kHz) into the cell. We take full scans of the probe detuning δ at different times t after the LIAD pulse (see Supplemental Material [25]). The time-resolved transmission $T(t, \delta)$ of the probe laser is used to calculate the change of the optical depth ΔOD. For every detuning, the transmission before the LIAD pulse is used as the background signal $T_0(t < 0, \delta)$, which is used to calculate $\Delta\mathrm{OD}(t, \delta) = \ln(T_0/T)$. Thereby the optical depth caused by the background vapor pressure is subtracted. A map of the time- and detuning-resolved ΔOD is shown in Fig. 2(a).

At $t = 0$ ns the LIAD pulse hits the cell and increases the optical depth. The time resolution of the measurements is limited by the time jitter of the LIAD pulse (500 ps) and the single-photon counting module (350 ps).

First, we focus on a thicker part of the cell [$L = 6.24(7)$ μm], where we measure a time- and detuning-resolved ΔOD map of the ^{85}Rb $F_g = 2$ transition of the D_2 line [Fig. 2(a)]. The transition is defined by the total angular quantum number F_g of the ground state g, while the total hyperfine splitting δ_{hfs} of the excited state cannot be resolved due to transient and Doppler broadening. The atoms moving in the laser propagation direction, originating from the entry facet of the cell, are probed at blue detunings $\delta > 0$. A second group of atoms, originating from the exit facet, is visible and probed at red detunings $\delta < 0$. The signal is higher for the atoms moving in the laser propagation direction. This asymmetry is not anticipated, but might originate from differences in the surface properties as it was observed in other experiments, i.e., depending on the coating [21]. We checked this hypothesis by rotating the cell by 180°, which led to a roughly inverted asymmetry. The darker region around zero detuning shows that fewer atoms with low z velocity are desorbed. In total, we measure two atom clouds moving toward the opposite cell walls. The high ΔOD value in the first nanoseconds is caused by a high atomic density and decreases over time. The ΔOD signal equilibrates to zero before the next LIAD pulse arrives. The dashed green lines indicate the time-of-flight curves, after which the atoms with a certain detuning hit the other cell wall according to $\mathrm{TOF}(\delta) = Lk/|\delta|$, with $\delta = \boldsymbol{k} \cdot \boldsymbol{v} \pm \delta_{\mathrm{hfs}}/2 = k v_z \pm \delta_{\mathrm{hfs}}/2$, respecting the hyperfine splitting of the excited state. There, $\boldsymbol{k}$ is the

wave vector of the probe beam, which is parallel to the z axis, $k = |\boldsymbol{k}|$ is the wave number of the probe beam, $\boldsymbol{v}$ is the velocity of the atom, and v_z is the z component of the velocity. We observe distinct signal wings beyond the respective time-of-flight curves indicating potential re-emission of atoms after arriving at the opposite cell wall.

Using this measurement as a reference, we develop a kinematic model and run a Monte Carlo simulation of atoms flying through a cell and interacting with the probe laser (see Supplemental Material [25]). The idea is to model the velocity distribution of desorbed atoms and to estimate the local density during the simulation.

In the model, the local and temporal desorption-rate scales linearly with the intensity of the LIAD pulse. For the velocity distribution, we assume $f(v, \varphi, \theta) = [4/(\sqrt{\pi}a^3)v^2 \exp(-v^2/a^2)]\cos(\theta)$ with the parameter a and the speed $v = |\boldsymbol{v}|$. The azimuthal angle φ is uniformly distributed, while the polar angle θ is distributed according to the $\cos(\theta)$-Knudsen law [31]. This simple distribution leads to a good qualitative agreement between measurement [Fig. 2(a)] and simulation [Fig. 2(b)]. We also assume that the atoms are desorbed only during the LIAD pulse and that there is no thermal desorption after the pulse, which is in good agreement with our measurement. Since no other mechanism (i.e., through natural or transit broadening, which are also included in the model) reproduces the signal wings beyond the time-of-flight curves (dashed green lines in Fig. 2), they might occur because of re-emissions from the surfaces after bombardment with the initial atom clouds. To get better agreement, an instant re-emission probability of 84% is included in the kinematic model.

The remaining discrepancies between measurement and simulation can originate from an inadequate velocity distribution model, intricate re-emission properties, additional decay mechanisms, the neglected Gaussian intensity distribution of the probe beam, and the use of the steady-state cross section of the atoms at all the times. Nevertheless, with the overall acceptable agreement between measurement and simulation we obtain a time- and z-dependent simulated local density, which shows that the desorbed atoms are initially in two flat, "pancakelike" clouds with an initial thickness well below the wavelength of the probe laser, rendering this into a 2D geometry (see Supplemental Material [25]).

To investigate high-density regimes, we use a thinner part of the cell, as the background optical depth and the detection limit of the single-photon counting module are limiting the measurement in the thicker part of the cell. We perform measurements at a cell thickness of $L = 0.78(2)$ μm at low and high atomic densities using the D_2 transition as shown in Figs. 3(a) and 3(b), respectively. Our measurements are in a regime where the total number of desorbed atoms per pulse monotonically increases with the peak intensity of the LIAD pulse (see Supplemental Material [25]). The low-density measurement corresponds

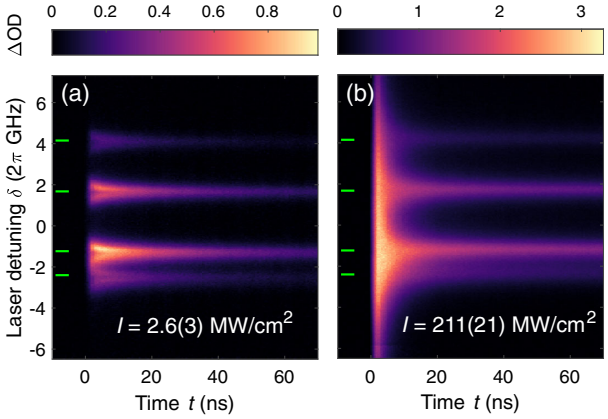

FIG. 3. Measurements of the time- and detuning-resolved ΔOD for low density (a) and high density (b) at the D_2 transition. There is a broadening and line shift of the spectrum in the first few nanoseconds for the high-density case. The measured broadening is mainly attributed to the density-dependent self-broadening (Γ_{self}). The line shift occurs due to the dipole-dipole shift (Δ_{dd}, more visible in the slices presented in the Supplemental Material [25]). The four green markers indicate the ground-state hyperfine splitting of the two isotopes of rubidium, respectively. The intensities I are the peak intensities of the LIAD pulse, the cell thickness is $L = 0.78(2)$ μm, and the reservoir temperature is $T_{\mathrm{res}} \approx 180\,^{\circ}\mathrm{C}$.

to a peak intensity of $I = 2.6(3)$ MW cm^{-2}, while the high-density case corresponds to $I = 211(21)$ MW cm^{-2}.

There is a broadening and line shift of the D_2 hyperfine transitions present in Fig. 3(b), which we attribute to density-dependent dipole-dipole interactions. The four peaks correspond to the ground state hyperfine splitting of the two isotopes of rubidium, contributing to the signal, while the hyperfine splitting of the excited state cannot be resolved. The density-dependent self-broadening [3,6] in the steady-state regime was predicted to be

$$\Gamma_{\mathrm{self}} = \beta_i n = \frac{2}{3\hbar\epsilon_0}\sqrt{\frac{g_g}{g_e}}d_J^2 n, \tag{1}$$

where β_i is the self-broadening coefficient, i enumerates the D_1 or D_2 transition, $\hbar$ is the reduced Planck constant, ϵ_0 is the vacuum permittivity, g_g and g_e are the multiplicities (depending on the quantum number J) of the ground and excited state respectively, d_J is the total reduced dipole matrix element, and n is the atomic density. In the high-density regime in Fig. 3(b) we observe a self-broadening of $\Gamma_{\mathrm{self}} \approx 590\Gamma_0$ at $t = 2$ ns, where $\Gamma_0 \approx 2\pi \times 6.07$ MHz [32] is the natural decay rate of the D_2 transition.

Similarly, we compare the line shift, observed in our measurements, to the steady-state dipole-dipole shift [5,7], which was predicted to be

$$\Delta_{\mathrm{dd}} = -|\Delta_{\mathrm{LL}}| + \frac{3}{4}|\Delta_{\mathrm{LL}}|\left(1 - \frac{\sin 2kL}{2kL}\right), \tag{2}$$

with Δ_{LL} being the Lorentz-Lorenz shift and L being the cloud thickness. This thickness dependency is a cavity-induced correction, also known as the collective Lamb shift. The Lorentz-Lorenz shift [5,7], in turn, is density dependent and can be written as

$$\Delta_{\mathrm{LL}} = -\frac{1}{3\hbar\epsilon_0} d_J^2 n. \tag{3}$$

As our cell thickness is $L \approx \lambda$, the second term of the dipole-dipole shift has a significant effect on the line shift and reduces the dipole-dipole effect to $\Delta_{\mathrm{dd}} \approx -\frac{1}{4}|\Delta_{\mathrm{LL}}|$. In the high-density measurement in Fig. 3(b) this corresponds to a value of $\Delta_{\mathrm{dd}} \approx -80\Gamma_0$ (redshift) at $t = 2$ ns. Additionally, we can observe that the transient density-dependent effects occur on a timescale of a few nanoseconds, which is faster than the natural lifetime of the D_2 transition (26.2 ns) [32].

To further investigate the dipole-dipole origin of the observed interaction, we compare the transient evolution of the self-broadening and line shift at the D_1 and D_2 transition of rubidium. We fit both measured data with a steady-state electric susceptibility model at each time step, using the software ElecSus [33]. The fits to the individual time-resolved spectra show a $< 6\%$ overall normalized root-mean-square deviation and result in the self-broadening and line shift shown in Figs. 4(a) and 4(b), respectively. Note that in the first 2 ns we cannot properly fit the data to this model, so we exclude these data points. The error bars represent the 1σ standard fit error (see Supplemental Material [25]). If we assume that the self-broadening and the line shift, according to the aforementioned steady-state equations, linearly depend on the density, we can calculate a peak density on the order of 10^{16} cm^{-3} using Eqs. (1) and (2).

There is an apparent difference of the self-broadening and line shift between the two transitions of rubidium, which can be attributed to different transition dipole matrix elements d_J. While it is not possible to conclusively deduce any precise value for d_J from our data, we calculate ratios between the D_1 and D_2 broadening and shift for otherwise identical measurements, which are shown in Figs. 4(a) and 4(b) on the right vertical axis. These values approach the ratios $\sqrt{1/2}d_{J,D_2}^2/d_{J,D_1}^2$ and $d_{J,D_2}^2/d_{J,D_1}^2$ emerging from Eq. (1) and Eq. (2), respectively, for large t as indicated by the black triangles. Deviations during the first $\approx$ 10 ns in the case of the self-broadening likely originate from limited accuracy of the fits with signal wings not captured with the scanned detuning range, asymmetries in the spectral profiles similar to what was reported in Ref. [8], or asymmetries from both hyperfine splitting and velocity distribution (see Fig. S4, Supplemental Material [25]). In contrast, the measured line shift is always much smaller than the scan range while almost vanishing for $t > 8$ ns such that the error bars are larger than the values

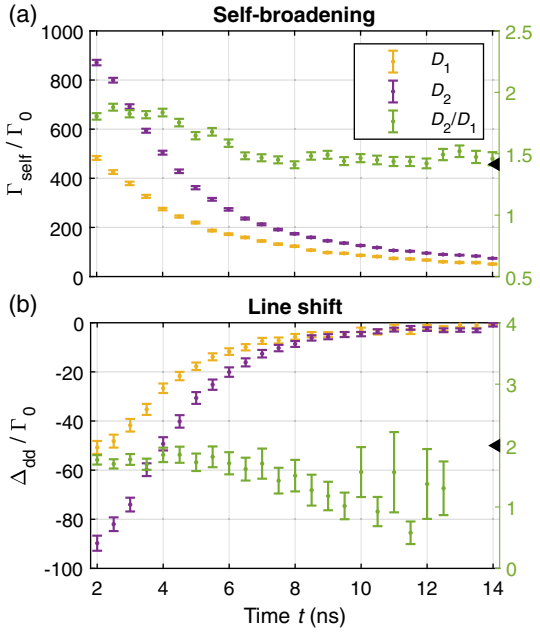

FIG. 4. (a) Time-dependent self-broadening Γ_{self} of the Rb spectra for the D_1 (yellow data) and D_2 (purple data) transition. The experiments are performed under identical conditions, except the probe laser wavelength. The ratio (green data) of the self-broadening of the two transitions approaches the theoretical steady-state ratio for large t (black triangle). Vertical error bars for $t < 8$ ns are likely underestimated due to a systematic effect, and horizontal precision is bandwidth limited by jitter. (b) Time-dependent line shift Δ_{dd} of the D_1 and D_2 transition. The ratio of the line shift, which is close to the theoretical value, has an increasing error for increasing time, and therefore the last three data points were omitted. The peak intensity of the LIAD pulse is $I = 317(32)$ MW cm^{-2}. The cell thickness is $L = 0.78(2)$ μm, and the reservoir temperature is $T_{\mathrm{res}} \approx 180$ °C.

themselves. Such systematic uncertainties are not properly captured by the standard errors as derived from the employed fitting algorithms.

In conclusion, we implemented a pulsed LIAD method to switch atom densities from 10^{14} cm^{-3} to more than 10^{16} cm^{-3} on a nanosecond timescale in a micrometer-sized cell. At high densities with $nk^{-3} \approx 100$ we are able to study the dipole-dipole induced self-broadening and Lorentz-Lorenz shift. Our measurements show that the interaction builds up faster than 2 ns, a timescale much shorter than the natural lifetime. The scaling between the D_1 and D_2 transition in the measurement supports the assumption that we observed dipolar effects in good agreement with the established theory. Overall, we do not see significant transient internal dynamics other than the one induced by the density change itself, since the motional dephasing is the fastest timescale equilibrating the shift and broadening of the many-body dynamics with dipolar interactions within $\approx$ 1 ns. With a better temporal resolution (e.g., with superconducting single-photon detectors) and shorter desorption pulses, it will be possible to

study the behavior of the transient dipole-dipole interaction in the first 2 ns, a regime which was not accessible in this Letter. The switching of the atomic medium by LIAD can be used with integrated photonic structures [34,35], e.g., to realize large optical nonlinearities at a GHz bandwidth for switchable beam splitters, routers, and nonlinear quantum optics based on the excitation blockade.

The supporting data for this article are openly available from [25] and [36]. Additional data (e.g., raw data of the time tagger) are available on reasonable request.

The authors thank Artur Skljarow for extensive support during the preparation of the final version of this Letter. This Letter is supported by the Deutsche Forschungsgemeinschaft (DFG) via Grant No. LO 1657/7-1 under DFG SPP 1929 GiRyd. We also gratefully acknowledge financial support by the Baden-Württemberg Stiftung via Grant No. BWST_ISF2019-017 under the program Internationale Spitzenforschung. H. A. acknowledges the financial support from Eliteprogramm of Baden-Württemberg Stiftung, Graduiertenkolleg "Promovierte Experten für Photonische Quantentechnologien" via Grant No. GRK 2642/1, and Purdue University startup grant. C. S. A. acknowledges support from EPSRC Grant No. EP/R002061/1.

F. C., M. M., and F. M. contributed equally to this work.

*t.pfau@physik.uni-stuttgart.de

[1] M. D. Lukin, M. Fleischhauer, R. Cote, L. M. Duan, D. Jaksch, J. I. Cirac, and P. Zoller, Dipole Blockade and Quantum Information Processing in Mesoscopic Atomic Ensembles, Phys. Rev. Lett. **87**, 037901 (2001).

[2] L. A. Williamson, M. O. Borgh, and J. Ruostekoski, Superatom Picture of Collective Nonclassical Light Emission and Dipole Blockade in Atom Arrays, Phys. Rev. Lett. **125**, 073602 (2020).

[3] E. Lewis, Collisional relaxation of atomic excited states, line broadening and interatomic interactions, Phys. Rep. **58**, 1 (1980).

[4] W. E. Lamb, Jr. and R. C. Retherford, Fine structure of the hydrogen atom by a microwave method, Phys. Rev. **72**, 241 (1947).

[5] R. Friedberg, S. Hartmann, and J. Manassah, Frequency shifts in emission and absorption by resonant systems of two-level atoms, Phys. Rep. **7**, 101 (1973).

[6] L. Weller, R. J. Bettles, P. Siddons, C. S. Adams, and I. G. Hughes, Absolute absorption on the rubidium D_1 line including resonant dipole–dipole interactions, J. Phys. B **44**, 195006 (2011).

[7] J. Keaveney, A. Sargsyan, U. Krohn, I. G. Hughes, D. Sarkisyan, and C. S. Adams, Cooperative Lamb Shift in an Atomic Vapor Layer of Nanometer Thickness, Phys. Rev. Lett. **108**, 173601 (2012).

[8] T. Peyrot, Y. R. P. Sortais, A. Browaeys, A. Sargsyan, D. Sarkisyan, J. Keaveney, I. G. Hughes, and C. S. Adams, Collective Lamb Shift of a Nanoscale Atomic Vapor Layer within a Sapphire Cavity, Phys. Rev. Lett. **120**, 243401 (2018).

[9] H. Dobbertin, R. Löw, and S. Scheel, Collective dipole-dipole interactions in planar nanocavities, Phys. Rev. A **102**, 031701(R) (2020).

[10] V. Lorenz, X. Dai, H. Green, T. Asnicar, and S. Cundiff, High-density, high-temperature alkali vapor cell, Rev. Sci. Instrum. **79**, 123104 (2008).

[11] A. Gozzini, F. Mango, J. H. Xu, G. Alzetta, F. Maccarrone, and R. A. Bernheim, Light-induced ejection of alkali atoms in polysiloxane coated cells, Il Nuovo Cimento D **15**, 709 (1993).

[12] M. Meucci, E. Mariotti, P. Bicchi, C. Marinelli, and L. Moi, Light-induced atom desorption, Europhys. Lett. **25**, 639 (1994).

[13] E. B. Alexandrov, M. V. Balabas, D. Budker, D. English, D. F. Kimball, C.-H. Li, and V. V. Yashchuk, Light-induced desorption of alkali-metal atoms from paraffin coating, Phys. Rev. A **66**, 042903 (2002).

[14] K. Ręblas and M. J. Kasprowicz, Reexamination of the theory of light-induced atomic desorption, Phys. Rev. A **79**, 042903 (2009).

[15] P. A. Petrov, A. S. Pazgalev, M. A. Burkova, and T. A. Vartanyan, Photodesorption of rubidium atoms from a sapphire surface, Opt. Spectrosc. **123**, 574 (2017).

[16] E. Talker, P. Arora, R. Zektzer, Y. Sebbag, M. Dikopltsev, and U. Levy, Light-Induced Atomic Desorption in Microfabricated Vapor Cells for Demonstrating Quantum Optical Applications, Phys. Rev. Applied **15**, L051001 (2021).

[17] P. F. Griffin, K. J. Weatherill, and C. S. Adams, Fast switching of alkali atom dispensers using laser-induced heating, Rev. Sci. Instrum. **76**, 093102 (2005).

[18] B. P. Anderson and M. A. Kasevich, Loading a vapor-cell magneto-optic trap using light-induced atom desorption, Phys. Rev. A **63**, 023404 (2001).

[19] S. N. Atutov, R. Calabrese, V. Guidi, B. Mai, A. G. Rudavets, E. Scansani, L. Tomassetti, V. Biancalana, A. Burchianti, C. Marinelli, E. Mariotti, L. Moi, and S. Veronesi, Fast and efficient loading of a Rb magneto-optical trap using light-induced atomic desorption, Phys. Rev. A **67**, 053401 (2003).

[20] C. Klempt, T. van Zoest, T. Henninger, O. Topic, E. Rasel, W. Ertmer, and J. Arlt, Ultraviolet light-induced atom desorption for large rubidium and potassium magneto-optical traps, Phys. Rev. A **73**, 013410 (2006).

[21] S. Ghosh, A. R. Bhagwat, C. K. Renshaw, S. Goh, A. L. Gaeta, and B. J. Kirby, Low-Light-Level Optical Interactions with Rubidium Vapor in a Photonic Band-Gap Fiber, Phys. Rev. Lett. **97**, 023603 (2006).

[22] A. D. Slepkov, A. R. Bhagwat, V. Venkataraman, P. Londero, and A. L. Gaeta, Generation of large alkali vapor densities inside bare hollow-core photonic band-gap fibers, Opt. Express **16**, 18976 (2008).

[23] A. Burchianti, A. Bogi, C. Marinelli, C. Maibohm, E. Mariotti, and L. Moi, Reversible Light-Controlled Formation and Evaporation of Rubidium Clusters in Nanoporous Silica, Phys. Rev. Lett. **97**, 157404 (2006).

[24] F. Ripka, H. Kübler, R. Löw, and T. Pfau, A room-temperature single-photon source based on strongly interacting Rydberg atoms, Science **362**, 446 (2018).

[25] See Supplemental Material at http://link.aps.org/supplemental/10.1103/PhysRevLett.128.173401 for additional details on the experimental setup, evaluation and the kinematic model, which additionally includes Refs. [26–30].
[26] N. Sekiguchi, T. Sato, K. Ishikawa, and A. Hatakeyama, Spectroscopic study of a diffusion-bonded sapphire cell for hot metal vapors, Appl. Opt. **57**, 52 (2018).
[27] R. Loudon, *The Quantum Theory of Light* (Oxford University Press, Oxford, 2000).
[28] D. A. Steck, Rubidium D Line Data, available online http://steck.us/alkalidata (revision 2.2.2, 9 July 2021).
[29] M. Knudsen, *The Kinetic Theory of Gases. Some Modern Aspects* (Methuen & Co., London, 1934).
[30] N. Šibalić, J. D. Pritchard, C. S. Adams, and K. J. Weatherill, ARC: An open-source library for calculating properties of alkali Rydberg atoms, Comput. Phys. Commun. **220**, 319 (2017).
[31] G. Comsa and R. David, Dynamical parameters of desorbing molecules, Surf. Sci. Rep. **5**, 145 (1985).
[32] U. Volz and H. Schmoranzer, Precision lifetime measurements on alkali atoms and on helium by beam–gas–laser spectroscopy, Phys. Scr. **T65**, 48 (1996).
[33] M. A. Zentile, J. Keaveney, L. Weller, D. J. Whiting, C. S. Adams, and I. G. Hughes, ElecSus: A program to calculate the electric susceptibility of an atomic ensemble, Comput. Phys. Commun. **189**, 162 (2015).
[34] R. Ritter, N. Gruhler, H. Dobbertin, H. Kübler, S. Scheel, W. Pernice, T. Pfau, and R. Löw, Coupling Thermal Atomic Vapor to Slot Waveguides, Phys. Rev. X **8**, 021032 (2018).
[35] H. Alaeian, R. Ritter, M. Basic, R. Löw, and T. Pfau, Cavity QED based on room temperature atoms interacting with a photonic crystal cavity: A feasibility study, Appl. Phys. B **126**, 25 (2020).
[36] F. Christaller, M. Mäusezahl, F. Moumtsilis, A. Belz, H. Kübler, H. Alaeian, C. S. Adams, R. Löw, and T. Pfau, Data for "Transient density-induced dipolar interactions in a thin vapor cell", Zenodo, 10.5281/zenodo.6411102 (2022).